

Design and analysis of an untethered micro flapping robot which can glide on the water

CHEN YanHong[†], LIU YiDe[†], LIU TaiShan, LI Hua, QU ShaoXing^{*} & YANG Wei

State Key Laboratory of Fluid Power & Mechatronic System, Key Laboratory of Soft Machines and Smart Devices of Zhejiang Provinces, Center for X-Mechanics, Department of Engineering Mechanics, Zhejiang University, Hangzhou 310027, China

Received February 17, 2022; accepted April 21, 2022; published online July 20, 2022

Flapping-wing flying insects possess various advantages, such as high agility and efficiency. The design and manufacture of insect-scale flapping-wing micro aerial vehicle (FWMAV) have attracted increasing attention in recent decades. Due to the limitations of size and weight, the FWMAV with an onboard battery which can fully mimic insect flight has not been achieved. In this work, we design and fabricate a highly integrated flapping-wing microrobot named Robomoth. The Robomoth consists of a carbon chassis, customized power and control devices, and two piezoelectric ceramic actuators symmetrically distributed in the thorax and controlled individually. It weighs 2.487 g, spans 5.9 cm in length, possesses 9 cm of wingspan, and carries a 0.355 g rechargeable lithium battery. We demonstrate the mobility of the Robomoth through untethered gliding and making turns on the water surface. A simplified dynamic model of the flapping system is proposed to explain the relationship between the driving frequency and the flapping amplitude. The Robomoth is one new untethered bioinspired flapping-wing robot that can perform stable water surface motion, which holds potential applications such as search and rescue on the water. The robot can also provide insight for designing insect-scale flying vehicles.

micro/nanorobots, biologically inspired robots, flapping-wing flying, piezoelectric ceramic actuator

Citation: Chen Y H, Liu Y D, Liu T S, et al. Design and analysis of an untethered micro flapping robot which can glide on the water. *Sci China Tech Sci*, 2022, 65, <https://doi.org/10.1007/s11431-022-2064-9>

1 Introduction

Creating flapping-wing aerial vehicles to mimic birds and insects has attracted many researchers in recent decades. The first electrically powered palm-sized flapping-wing aerial vehicle was developed in 2001 [1]. Since that, designing flapping-wing vehicles has remained an attractive research topic in the field of robotics, and varieties of prototypes have been constructed. Compared with traditional aerial vehicles, flapping-wing aircraft exhibits the properties such as small size, low flight Reynolds number, and unsteady aerodynamic characteristics [2–4]. Meanwhile, the agility and high man-

euverability of flapping-wing flying robots give them the potential to perform various tasks such as pollination, exploration of the confined space, and search and rescue after the earthquake. So far, flapping-wing aerial vehicles generally take inspiration from hummingbirds [5,6], bats [7,8], dragonflies [9], bees [10–14], and flies [15–18]. It is not a hard problem for those flapping-wing aerial vehicles with relatively large sizes to achieve untethered flight due to the large load capacity and ample design space. For flapping-wing micro aerial vehicle (FWMAV), however, the untethered flight with onboard power and control system is still one of the grand challenges, which leads to limited applications.

The design and manufacture of FWMAV should consider the requirements and restrictions of the subsystems. The key

[†]These authors contribute equally to this work.

^{*}Corresponding author (email: squ@zju.edu.cn)

challenge is to balance the trade-off among all subsystems, such as driven systems, transmission mechanisms, and electronics. Though the previous studies have extensively investigated the motor actuators and electromagnetic actuators on FWMAV [6,8,19–28], controlling stroke amplitude, duty cycle, and mean stroke plane of the motor-driven flapping system with limited volume and weight is still difficult due to the slow advances on control mechanisms and feedback systems [29–31]. Smart materials such as piezoelectric ceramics [16,32] and dielectric elastomers [14] have raised attention due to their large deformation, low weight, small size, and high driving frequency.

The transmission mechanism design highly depends on the actuator. It converts the output of the actuator into the flapping or twisting of the wings. Gear rocker mechanisms are often introduced as transmission mechanisms for the motor actuator. For electromagnetic motor and smart material actuators, researchers developed a smart composite microstructure (SCM) method [33] to create a linkage mechanism with micro flexure hinges, which can convert and amplify the deformation. One of the highlights of the insect and bird flight is that the flapping motion has multiple degree(s) of freedom (DoF). For instance, the wings can twist or swing back and forth [34–37]. How to achieve this natural behavior is one of the major concerns in robot design. Researchers have successfully achieved two DoFs flapping control on the micro-flapping wing mechanism, namely flapping and twisting or flapping and deviation [38–41]. It is, however, heavier and consumes more space compared with one DoF robot. In the Harvard Robobee series, researchers have achieved the twist motion of the flapping wing by using the passive hinge rather than active 2-DoF flapping [32]. Meanwhile, to get rid of the mass limit of the battery, the researchers successfully achieved the untethered flight of the FWMAV by using photovoltaic power, which marks an enormous advance [12,16].

In this paper, we present a new design of the insect-scale flapping-wing robot. The robot weighs 2.487 g, spans 6 cm in length, and carries a 0.355 g rechargeable lithium battery. The wingspan of the robot is 9 cm, and the robot is named Robomoth. The Robomoth is fabricated through the SCM method and equipped with wireless onboard power and control system (Figure 1). It is driven by a pair of piezoelectric ceramic bending actuators, which generates thrust force and drives untethered gliding on the water. The thrust force of the robot is measured, and the mobility of the robot on the water surface is characterized. A simplified dynamic model of the flapping system is proposed to explain the relationship between the driving frequency and the flapping amplitude. The Robomoth is the first untethered bioinspired flapping-wing robot that can perform stable water surface movement, holding potential applications such as search and rescue on the water. Further-

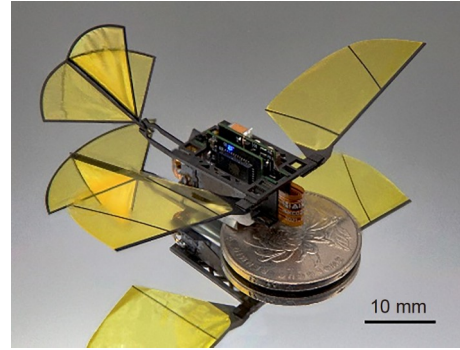


Figure 1 (Color online) Robomoth: a 2.487 g flapping-wing microrobot capable of untethered gliding on water.

more, this work can provide insight for designing insect-scale flying vehicles.

2 Design and fabrication

This work intends to design and manufacture an insect-scale flapping-wing robot with a mass limitation of 3 g and a wingspan less than 10 cm, which can be equipped with on-board power and control devices. To achieve this goal, it is necessary to design the subsystems such as actuators, transmission mechanisms, wings, power supply, and integrated structures. Since the flapping-wing robot is a complicated system, the subsystems affect each other and define the overall performance of the robot. The main parts of the Robomoth are made and assembled by the SCM method, as shown in Figure 2.

All components of the SCM method for constructing the mechanisms, actuators, and wings are listed in Table 1.

2.1 Actuators

The geometry of the actuator requires a comprehensive consideration of the load capacity of the power supply and the dynamic response characteristics of the driving system. Limited by the energy density of the actuator and mass requirement of the robot design, the actuator should neither be too large to lean on much energy consumption and heavy electronic devices, nor too small to cause the low actuation ability and weak flapping performance. In this work, the actuator is designed as 13 mm in length, with a trapezoid shape to minimize the torque distribution unbalance. The top width of the actuator is 1.7 mm and the bottom width is 6 mm. To make the robot more compact, the actuator is made into an inclined asymmetric shape and placed symmetrically on both sides of the thorax of the robot.

We chose PZT-5H ceramics to fabricate the composite piezoelectric ceramic bending actuator. Firstly, we place the pre-cut piezoelectric ceramics and alumina ceramics in the

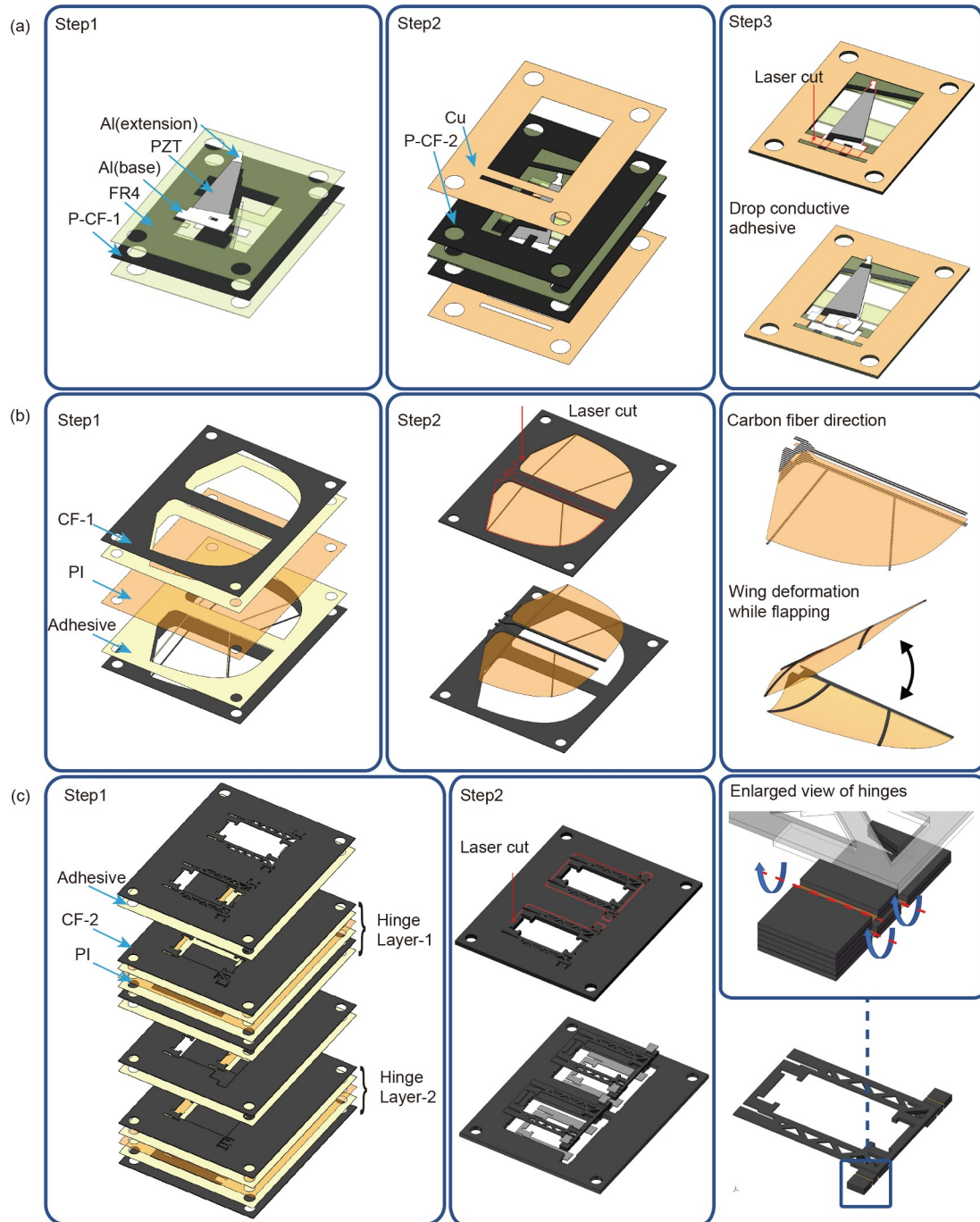


Figure 2 (Color online) The fabrication process of actuators, wings, and transmission of Robomoth. (a) Fabrication process of the actuator. In Step1, all ceramic and carbon fiber layers are bonded by heat pressing. In Step2, electrodes are formed by heat pressing. The whole actuator is released by laser cutting and dropping conductive adhesive in Step3. (b) Fabrication process of the flexible wing. All the carbon fiber, adhesive, and polyimide membranes are bonded by heat pressing in Step1 and the wing is released in Step2. The direction of carbon fiber and the way it deforms are illustrated. (c) Fabrication process of transmission. The process is similar to the process in (b) and the enlarged view of hinges is shown in the inset.

FR4 frame, and the carbon fiber prepreg in the middle is aligned with the FR4 frame (Figure 2(a) Step1). The alumina ceramics is adopted to reinforce the actuator and facilitate the assembly process. After the first round of heat pressing, the carbon fiber and copper foil are attached to the stack. In addition to forming electrodes, this step can also strengthen

the bond between the piezoelectric ceramics and the alumina ceramics (Figure 2(a) Step2). After the second round of heat pressing, the actuator is released from the frame by laser cutting, and the middle carbon fiber layer and the surface electrodes are connected by conductive epoxy resin (Figure 2(a) Step3).

Table 1 Thickness of the components of the Robomoth

Component	Abbreviation	Thickness (μm)
Carbon fiber 1	CF-1	100
Carbon fiber 2	CF-2	200
DuPont FR1500 sheet adhesive	Adhesive	12.5
Polyimide film	PI	7.5
Epoxy glass cloth	FR4	127
Piezoelectric ceramic	PZT	127
Alumina ceramic	Al	200
Carbon fiber prepreg 1	P-CF-1	50
Carbon fiber prepreg 2	P-CF-2	200
Copper foil	Cu	13

2.2 Wings

The wings play an important role in the FWMAV for generating aerodynamic force. In addition, wing rotation during flapping is an important element [36]. There are many existing schemes to accomplish wing rotation, which can be classified as active and passive schemes. Rotating the wing actively at insect-scale would cause limitations such as complex design, confined space, and low weight. Accordingly, passive wing rotation is preferred for it leverages the flexibility of the wings. The existing passive wing rotation methods include flexure hinges [32], bistable wings [6], and flexible wings [24,42]. Passive hinge is not appropriate for horizontal flight for its lack of rigidity in supporting the weight and maintaining the angle of the attack of the wings. To resolve the above problems while allowing the wing rotation, the unidirectional carbon fiber is adopted to the wing's fabrication (CF-1). The direction of the carbon fibers is parallel to the direction of the leading edge, which benefits the stiffness of the wings for supporting the weight of wings while allowing the wings to rotate (Figure 2(b)). The membrane of the wings is a 5 μm thick polyimide (PI) film. The wings are released by laser cutting. Owing to the unidirectional carbon fiber, the wings can perform rotation motion under the action of inertia force and aerodynamic force. A tail wing is constructed via a similar process but is fully constrained by the carbon fiber frame thus unable to deform.

2.3 Transmission

The transmission mechanism converts the linear displacement of the actuator tip into the axial rotation of the wing. The SCM method is applied to manufacture a miniature slider-crank mechanism symmetrically, as shown in Figure 3.

The transmission ratio T (wing rotation angle divided by the tip deflection of the actuator) is about $1/l_1$ and can be adjusted by designing the length of l_1 . The fabrication pro-

cess is shown in Figure 2. Each mechanism has three flexible hinges, which are divided into two layers during fabrication. All sheets of the structure are patterned by laser and pressed into a multilayer deck (Figure 2(c) Step1). The deck is then cut by laser to release the body frame with two slider-crank transmission mechanisms (Figure 2(c) Step2, grey parts are discarded), with no additional assembly process required.

2.4 Power, control, and actuation

The Robomoth is actuated by two piezoelectric actuators and fabricated by the SCM method. To achieve the untethered locomotion, the onboard power and control electronics are equipped. A 3.7 V, 10 mAh rechargeable lithium battery is chosen as the power source for the robot. The onboard chip contains three parts, the micro-controller, the high voltage amplifier, and the transfer board. The micro-controller can receive the commands and adjust the output of the high voltage amplifier. To achieve the 2-DoF flight control, two piezoelectric actuators are placed on both sides of the Robomoth to actuate the wings individually. The simultaneous configuration [43] is adopted here to achieve the electrical contact. The passive flexible carbon fiber is embraced symmetrically by two active piezoelectric ceramics. The high voltage amplifier offers six wires: two 250 V bias wires, two ground wires, and two 0–250 V drive signal wires for driving the left side and the right side actuators by square waves independently.

Each piezoelectric actuator contains two PZTs and three electrodes (Figure 4). Since the simultaneous configuration is adopted here, the polarity direction of each ceramic is the same. The amplitude of the bending actuator is controlled by

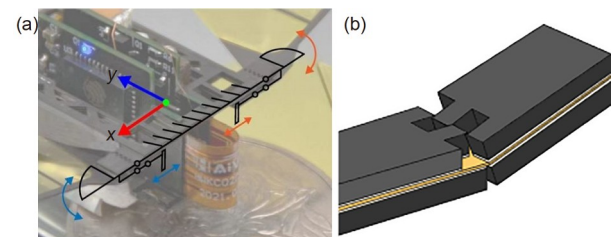


Figure 3 (Color online) (a) Transmission mechanism of the Robomoth. Each circle represents a flexible hinge in (b). Each axis of the hinge is parallel to the y direction.

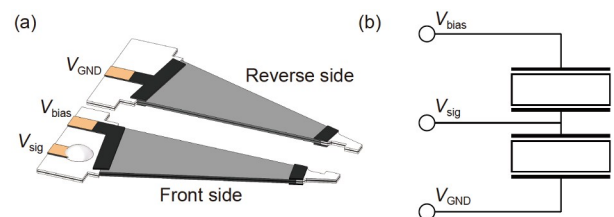


Figure 4 (Color online) (a) Electrical contacts of the PZT actuator. (b) Driving diagram of the PZT actuator.

altering V_{bias} , and the frequency is controlled by adjusting V_{sig} .

In summary, the Robomoth contains the carbon fiber structure and transmission, actuators, wings, battery, onboard chips, and some connecting wires and solder. The total mass of a Robomoth is 2.487 g.

The mass contributions of each part are listed in Table 2. The illustration of system integration of the Robomoth is shown in Figure 5.

3 Experiments and discussion

3.1 Characterizations of the PZT actuator

In this section, we measure the maximum free deflection of the PZT actuator. The drive signals are set as square waves and the test voltage ranges from 150 to 250 V. The test frequency ranges from 10 to 100 Hz. The free deflection of the actuator is captured by a laser sensor (LK-G30, KEYENCE). The results are plotted in Figure 6.

The shape of the deflection curve barely changes as the test frequency increases (Figure 6). We calculated the peak-to-peak displacement as the free deflection. A maximum free deflection of nearly 712 μm occurs at 60 Hz, 250 V. The free deflection drops as the voltage drops.

3.2 Thrust force test

In this section, we measure the thrust force of the Robomoth. The drive signals are set as a square wave and the test voltage ranges from 100 to 250 V. The test frequency ranges from 10 to 60 Hz. The wing membrane and stiffeners twist around the leading edge while flapping, which can be captured by a camera set vertically right above the Robomoth (Figure 7). The thrust force of the actuator is captured by a uniaxial force transducer (ULC-1N, INTERFACE). The results are plotted in Figure 8. The maximum thrust is 2.27 mN at 50 Hz, nearly 10% of its weight.

During downstroke, for example, the wing rotates around the leading edge in the opposite direction. At the end of the stroke, the wing reverses rapidly under the combination of aerodynamic force and inertial force, which generates aerodynamic lift effectively (Figure 7). The upstroke keeps the

Table 2 Mass distribution of the Robomoth

Part	Mass (g)
Structure and transmission	0.274
Piezoelectric actuator	0.356
Battery	0.355
Onboard chip	1.192
Wires, solder and glue	0.229
Wings	0.081
Total	2.487

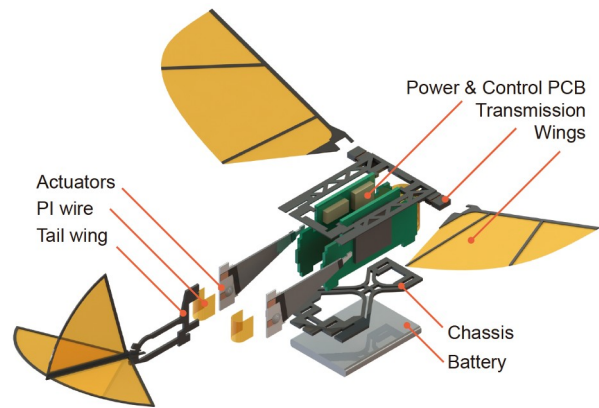


Figure 5 (Color online) Illustration of the system integration of the Robomoth.

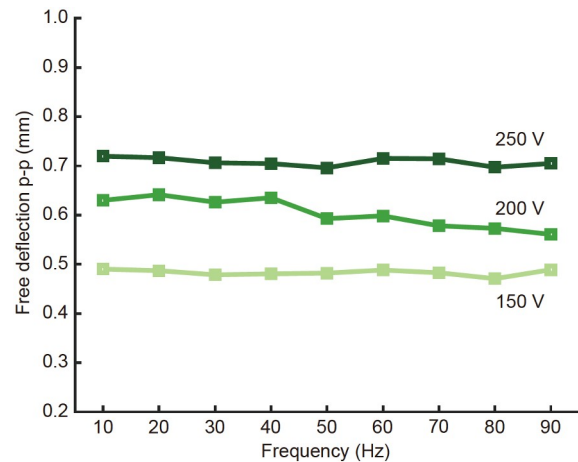


Figure 6 (Color online) The free deflection of the actuator under different driving signals.

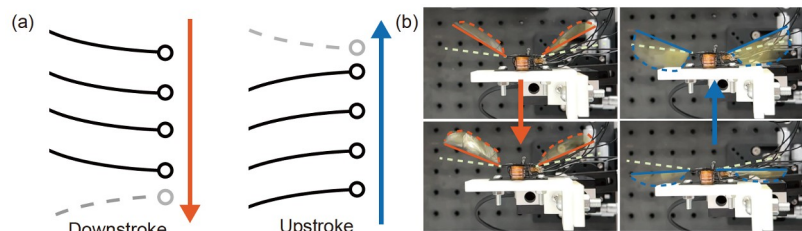


Figure 7 (Color online) Wing deformation while flapping. (a) Schematic diagram; (b) experiment snapshot.

same. Attributing to the flexible wing design, the resultant force is generated during flapping. The result indicates that the flexible wings made by unidirectional carbon fiber plate can sustain deformation and generate lift force effectively.

3.3 Gliding test

The water gliding test mainly aims at measuring the robot's velocity on the water by its thrust force. Some insects [44]

and FWMAV [45] can glide on the water by flapping wings. By adding an extra float platform under the chassis, the Robomoth can float on the water and glide straight forward or make turns by flapping. The gliding speed of the Robomoth driven by onboard electronics is tested with selected voltages of 150, 200, and 250 V. The test results are recorded in Figure 9(a) and (b). The maximum velocity is 17.1 cm/s occurring at 250 V, 40 Hz. By controlling the flapping frequency of two wings independently, the Robomoth can

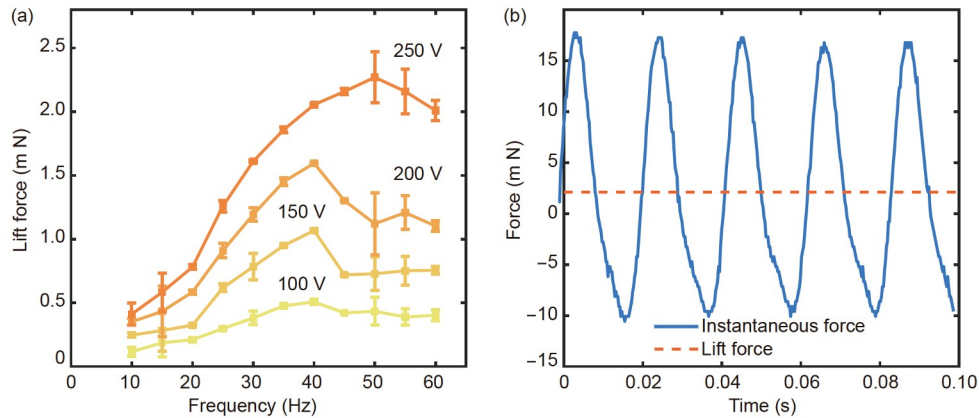


Figure 8 (Color online) (a) The lift forces under different driving signals. (b) Measured force vs. time curve at 45 Hz, 300 V. The lift force is calculated by taking the average of the instantaneous force over a five-second flapping cycle.

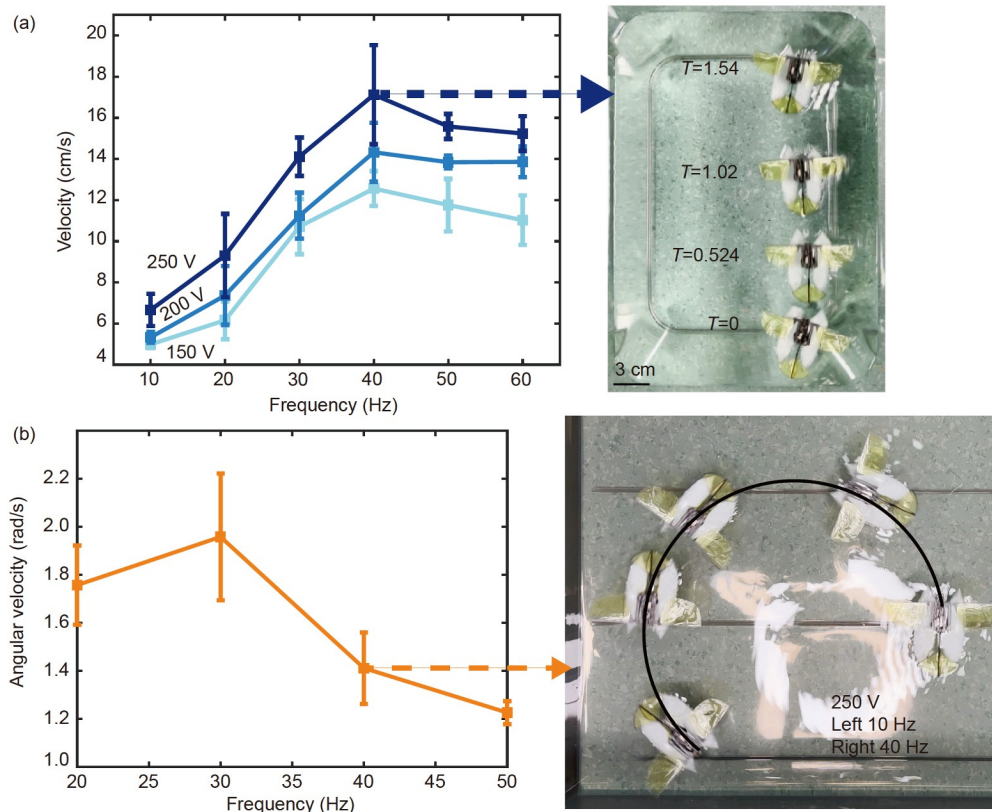


Figure 9 (Color online) (a) The glide velocities on water under different driving signals and four snapshots of the Robomoth glide on water at a maximum velocity. (b) The turning angular velocities on water under different driving frequencies and snapshots of experiment at 40 Hz.

generate the asymmetric lift force and make turns on the water. To make a left turn, for example, we set the drive signal of the left actuator as 250 V, 10 Hz and that of the right actuator as 250 V, 40 Hz. We test and record several groups of turning angular velocities under 250 V from 20 to 50 Hz for the right side and 10 Hz for the other side, respectively (Figure 9(b)). The maximum turning angular velocity is 1.96 rad/s at 250 V, 30 Hz. It should be emphasized that the maximum velocity and minimum turning radius are highly relevant to the shape of the floating platform and the contact between water and the platform.

3.4 Energy consumption

In this section, we measure the energy consumption of the Robomoth under different driving signals. In order to facilitate the measurement, we use a DC source as the power supply. The voltage remains constant at 3.7 V and we measure the current to get the power consumption. The results are displayed in Table 3. The results show that the maximum power consumption is 570.9 mW at 250 V, 50 Hz, which corresponds to the condition of the maximum lift force. It should also be noticed that when the robot is not flapping, the electric device consumes 160 mW for maintaining a wireless connection with the computer.

4 Dynamic model of the flapping system

During the mobility characterization, the flapping motion of the Robomoth draws our attention for its wing flapping amplitude drops as the driving frequency increases. The wing flapping amplitude drops sharply after 30 Hz. We conclude this phenomenon as the frequency-related response of the flapping system, which includes the piezoelectric ceramic actuator, the transmission mechanisms, and the wing design. To explain this phenomenon and to guide the future design of the flapping system, a simplified dynamic model is proposed and verified by the experiments.

4.1 Model description

The major demand for designing a flapping wing robot is to achieve desired flapping motion, especially the frequency and the amplitude. As for a flapping system driven by a piezoelectric ceramic actuator, the deflection of the actuator is generally converted into the flapping motion of the wings through the transmission mechanism. The piezoelectric ceramic actuator has a relatively high natural frequency, but its operating bandwidth decreases sharply after connecting the transmission mechanism to the wing. To get a clearer picture of this problem, we simplified the flapping system, as illustrated in Figure 10. For the convenience of calculation,

Table 3 Power consumption of the Robomoth

Frequency (Hz)	Current (mA)	Power (mW)
40	105.4	390.0
50	154.3	570.9
60	126.5	468.1

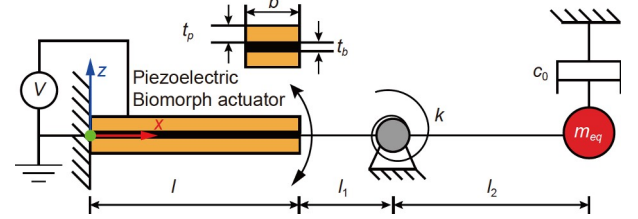


Figure 10 (Color online) Schematic of the flapping-wing system.

the trapezoidal actuator is simplified as a cantilever beam, and the transmission mechanism consisting of three flexible hinges is simplified as a torsion spring connected to the end of the cantilever beam through a rigid connecting rod. An equivalent mass and an additional linear damper are attached to the other end of the rod, and they represent the equivalent mass of the wing and the air damping effect, respectively. The simplified model ignores the structural damping and viscous damping [46] of the actuator itself, as well as the nonlinearity of the transmission mechanism. The resultant point of air resistance is assumed to overlap with the wing. In the simplified model, l represents the length of the actuator, t_p the thickness of the piezoelectric ceramic, t_b the middle carbon fiber passive layer thickness, b the width of the actuator, l_1 the transmission ratio, l_2 the distance between the center of gravity and the axis of rotation, k the bending modulus of the torsional spring, m_{eq} the equivalent mass of the wing, c_0 the air damping coefficient, and V the voltage applied to the upper layer of the driver, respectively. Since the actuation mode of the piezoelectric ceramic actuator is modelled by simultaneous configuration, the direction of the electric field applied to the ceramic plate does not change and only one ceramic plate is actuated. The way this signal is loaded is equivalent to the electric field with alternating voltage applied to only one ceramic plate. Thus, the differential vibration equation can be written as

$$\rho w_{tt} + E_0 w_{xxxx} = 0, \quad (1)$$

where w_{tt} and w_{xxxx} represent $\frac{\partial^2 w}{\partial t^2}$ and $\frac{\partial^4 w}{\partial x^4}$ for simplification.

The boundary conditions are

$$x = 0, \quad w = w_x = 0, \quad (2)$$

$$x = l, \quad E_0 w_{xx} + \frac{bh_{31}C_2}{t_p\beta_{33}}V = 0, \quad (3)$$

$$x = l, \quad E_0 w_{xxx} - \frac{m_{eq}l_2^2}{l_1^2}w_{tt} + \frac{bc_0l_2^2}{l_1^2}w_t + \frac{k}{l_1^2}w = 0. \quad (4)$$

The symbols E_0 , ρ and C_1 are defined in the same way as in ref. [47]:

$$E_0 = \frac{1}{12}c_b t_b^3 b + 2C_1, \quad \rho = b(\rho_b t_b + 2\rho_p t_p),$$

$$C_1 = \frac{1}{12}c_p t_p (3t_b^2 + 4t_p^2 + 6t_p t_b) b, \quad C_2 = \frac{1}{2}t_p (t_b + t_p),$$

where ρ_b and ρ_p represent the densities of the carbon fiber and the piezoelectric ceramic, c_b and c_p represent the Young's moduli of carbon fiber and piezoelectric ceramic, h_{31} and β_{33} represent the coupling coefficient and anti-dielectric constant of piezoelectric ceramic. The initial conditions are

$$t = 0, \quad w = w_i = 0. \quad (5)$$

Discretizing eq. (4) with an implicit scheme, we obtain

$$w_{i+2}^{j+1} - 4w_{i+1}^{j+1} + 6w_i^{j+1} - 4w_{i-1}^{j+1} + w_{i-2}^{j+1} + \frac{\Delta x^4 \rho}{EI} \frac{w_i^{j+1} - 2w_i^j + w_i^{j-1}}{\Delta t^2} = 0, \quad (6)$$

where w_i^j represents the deflection of the actuator at point i in time j , Δx and Δt represent the grid sizes of spatial and temporal discretizations. After introducing the boundary conditions (2)–(4) and the initial condition (5) into eq. (6), we obtain the numerical solution of the equation and then calculate the rotation angles at different times. All parameters needed are given in Table 4.

4.2 Experimental verification and discussion

The model is applied to the Robomoth for verification. We calculate the amplitude of the flapping-wing in response to the square wave with different frequencies based on the model above. To verify the results of the model, we perform the experiments on the Robomoth with identical parameter settings and the results are compared in Figure 11(a). The experimental results showed that when the frequency is applied under 30 Hz, the amplitude of the flapping-wing maintains at about 45 degrees. However, as the frequency

Table 4 Physical parameters

Parameter	Symbol	Value
Actuator length (cm)	l	13
Actuator width (cm)	b	2.8
PZT thickness (μm)	t_p	127
PZT density (kg/m^3)	ρ_p	7800
PZT modulus (GPa)	c_p	56
PZT coupling coefficient (V/m)	h_{31}	5×10^8
PZT anti-dielectric constant (m/F)	β_{33}	2.9×10^7
Carbon fiber thickness (μm)	t_b	50
Carbon fiber density (kg/m^3)	ρ_b	1500
Carbon fiber modulus (GPa)	c_b	230
Radius to center of gravity (cm)	l_2	12.5
Transmission length (mm)	l_1	0.45
Equivalent mass (mg)	m_{eq}	20
Air damping (mN m/s)	c_0	6
Equivalent spring constant ($\mu\text{N m/rad}$)	k	20

increases further, the angle drops sharply to about 15 degrees, which is hard to drive Robomoth. The model performs a similar trend.

Since the voltage signal applied here is a square wave, the actuator can be considered as subjected to impact load at each start of the period disregarding the frequency and voltage. At low frequency (≤ 30 Hz), the period is relatively long which leads to enough response time for the wing to achieve a stable amplitude. Thus, the flapping amplitude keeps stable at a low-frequency range which we call a plateau. As the frequency increases, the influence of the air damping increases accordingly. Before the wing reaches the expected position, the stroke changes lead to the dropping of the amplitude. This can explain the continuous decline of response at above 30 Hz.

To verify the model, another test is performed without the wing membrane. We measure the flapping amplitude of the

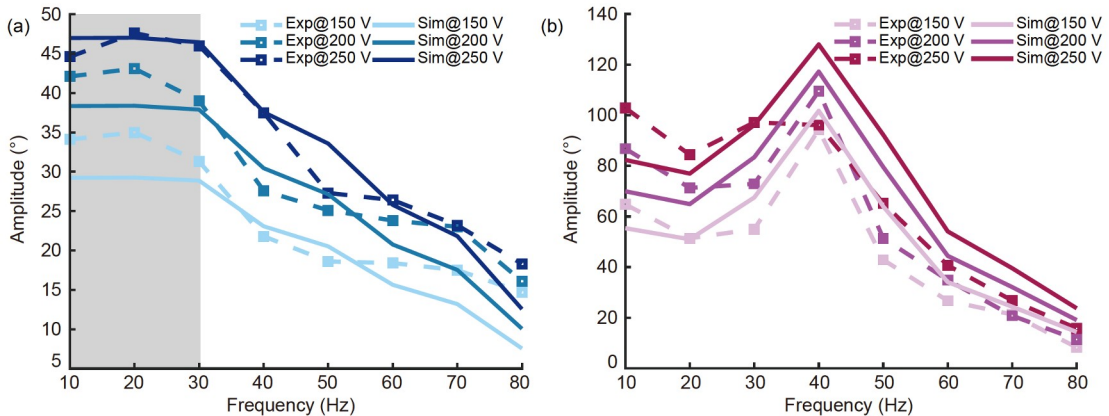


Figure 11 Simulation and experiment results of the flapping amplitude. (a) Flapping amplitude vs. frequency curve. (b) Flapping amplitude vs. frequency curve while the membrane of the wing is removed.

flapping system with only the carbon-fiber wing frame. Thus, the factor of the air damping effect in the model is removed. The results are compared in Figure 11(b). Without the air damping, the rotation angle increases considerably, and there is a resonant frequency at about 40 Hz both in experiment and simulation since the attached mass of the wing reduces the resonant frequency of this system.

The resonant frequency of the PZT actuator is relatively high (≈ 800 Hz) due to its low mass. The effective mass of the wing amplified by the transmission mechanism connecting with the actuator, however, is relatively large. That lowers the resonant frequency of the flapping system. Meanwhile, due to the constraint applied by the transmission mechanism, the resonant amplitude of the flapping system is limited while the simulation does not take into account this factor. Thus, minimizing the mass of the wing or reducing the transmission ratio can increase the resonant frequency of the flapping system in simulation. Compared with the former result with the membrane on the wing, the amplitude at low frequency is bigger in the absence of air damping. For the prescribed actuator and transmission mechanism, the larger size of the wing will lead to a smaller or even disappearing plateau frequency range, as well as minimize the maximum amplitude of flapping. Hence it is important to take both the air damping effect and size of the actuator into consideration while designing the large-wing flapping system. Besides, the stiffness of the transmission mechanism can slightly affect the performance of the flapping system which is observed in the experiments but not demonstrated in this paper.

The above experimental results and simulations reveal that the decrease in the flapping amplitude is mainly attributed to the influence of air damping. In addition, the mass of the wing and transmission ratio are important factors that influence the resonant frequency of the system. Under the mutual antagonism of increasing frequency and decreasing amplitude, the total lift force reaches a peak at 50 Hz. The geometry of the wing is the main factor affecting the air damping coefficient. A larger flexible wing leads to higher air damping and unsatisfactory performance in high frequency since larger wings generate larger aerodynamic force at the same stroke amplitude and frequency. Therefore, increasing the wing size blindly will make it difficult for the flapping system to achieve the expected performance. In this work, we optimized the wing shape and size according to the wing load and flexibility. Limited by the number of proto-

types, there is still great potential for making further optimization. While keeping the area of wings, we can adjust the stiffeners and the geometric shape of wings to make them easier to deform while flapping and generating larger aerodynamic force. Researchers also noticed that the inertial of wings play a critical role in the FWMAV [48], which leads to an important direction of optimization. Furthermore, we can use some numerical tools such as machine learning and CFD to make optimization more effective.

In this section, we present a simplified dynamic model of the flapping system, including a bending actuator, transmission mechanism, and wing to simulate the frequency response of a piezoelectric actuator flapping-wing robot. Comparison of the experimental and simulation results indicates that the model helps us estimate the performance of the system under different transmission ratios, sizes of the actuator, and sizes of the wing. Once the flapping amplitude and frequency are obtained through this dynamic model, CFD algorithms or software can be further applied to estimate the aerodynamic force.

5 Conclusion and future work

In this paper, Robomoth, a novel insect-like flapping-wing robot with onboard power and control devices, is presented. The Robomoth weighs 2.487 g with a wingspan of 9 cm. It contains a complete power supply system and untethered glide on the water at the maximum speed of 17.12 cm/s. Compared with wings with passive hinges, flexible wings achieve rotating motion under aerodynamic force and inertial force while avoiding the deformation caused by weight. A large wing design can minimize the wing load, which is beneficial to FWMAV with onboard power and control systems. The advantages of Robomoth are multi-degree control and power autonomy [49]. Attributed to two independent piezoelectric actuators, the Robomoth holds the ability to actively control roll, pitch, yaw, and thrust without additional control actuators and mechanisms. And the Robomoth is equipped with batteries that allow it to work independently of external energy sources which are described as power autonomy. Table 5 shows the comparison of untethered FWMAV. The mass and wingspan of Robomoth are the smallest among the untethered FWMAV with power autonomy.

Table 5 Comparison of untethered FWMAV

Project	Mass (g)	Wingspan (cm)	Maximum velocity (cm/s)	Mobility autonomy	Power autonomy
DelFly micro [20]	3.07	10	Not mentioned	No	Yes
Robofly [16]	0.19	≈ 3 (estimated)	Not mentioned	Yes	No
Robobee X-wing [12]	0.26	3.5	≈ 39.8 (estimated)	No	No
This work	2.49	9	17.1 (on the water)	Yes	Yes

To gain insights into the performance of the flapping wing system, a simplified dynamic model is proposed to simulate the frequency response. Comparison of the simulation and experimental results proves that the model can explain the phenomenon that the flapping amplitude decreases as the actuation frequency increases. This model can also be used to guide the design of the flapping system with desired flapping amplitude and frequency of the flapping-wing robot.

Future work will focus on promoting the aerodynamic performance of the Robomoth and optimizing the flapping system based on the dynamic model proposed here.

This work was supported by the National Natural Science Foundation of China (Grant No. 91748209), the 111 Project (Grant No. B21034), and the Key Research and Development Program of Zhejiang Province (Grant No. 2020C05010).

- 1 Pornsiri-sirirak T N, Tai Y, Ho C, et al. Microbat: A palm-sized electrically powered ornithopter. In: Proceedings of the NASA/JPL Workshop on Biomimetic Robotics, 2001. 17
- 2 Platzer M F, Jones K D, Young J, et al. Flapping wing aerodynamics: Progress and challenges. *AIAA J*, 2008, 46: 2136–2149
- 3 Bradshaw N, Lentink D. Aerodynamic and structural dynamic identification of a flapping wing micro air vehicle. In: Proceedings of the 26th AIAA Applied Aerodynamics Conference. Honolulu, Hawaii: American Institute of Aeronautics and Astronautics, 2008
- 4 Zhao L, Huang Q, Deng X, et al. Aerodynamic effects of flexibility in flapping wings. *J R Soc Interface*, 2010, 7: 485–497
- 5 Keennon M, Klingebiel K, Won H. Development of the nano hummingbird: A tailless flapping wing micro air vehicle. In: Proceedings of the 50th AIAA Aerospace Sciences Meeting Including the New Horizons Forum and Aerospace Exposition. Nashville, Tennessee: American Institute of Aeronautics and Astronautics, 2012. 588
- 6 Tu Z, Fei F, Deng X. Untethered flight of an at-scale dual-motor hummingbird robot with bio-inspired decoupled wings. *IEEE Robot Autom Lett*, 2020, 5: 4194–4201
- 7 Ramezani A, Shi X, Chung S J, et al. Bat Bot (B2), a biologically inspired flying machine. In: Proceedings of the 2016 IEEE International Conference on Robotics and Automation (ICRA). Stockholm, Sweden: IEEE, 2016. 3219–3226
- 8 Ramezani A, Chung S J, Hutchinson S. A biomimetic robotic platform to study flight specializations of bats. *Sci Robot*, 2017, 2: eaal2505
- 9 Dileo C, Deng X. Design of and experiments on a dragonfly-inspired robot. *Adv Robot*, 2009, 23: 1003–1021
- 10 Wood R J. Liftoff of a 60 mg flapping-wing MAV. In: Proceedings of the 2007 IEEE/RSJ International Conference on Intelligent Robots and Systems. San Diego: IEEE, 2007. 1889–1894
- 11 Pérez-Arancibia N O, Whitney J P, Wood R J. Lift force control of flapping-wing microrobots using adaptive feedforward schemes. *IEEE ASME Trans Mechatron*, 2013, 18: 155–168
- 12 Jafferis N T, Helbling E F, Karpelson M, et al. Untethered flight of an insect-sized flapping-wing microscale aerial vehicle. *Nature*, 2019, 570: 491–495
- 13 Chen Y, Helbling E F, Gravish N, et al. Hybrid aerial and aquatic locomotion in an at-scale robotic insect. In: Proceedings of the 2015 IEEE/RSJ International Conference on Intelligent Robots and Systems (IROS). Hamburg: IEEE, 2015. 331–338
- 14 Chen Y, Zhao H, Mao J, et al. Controlled flight of a microrobot powered by soft artificial muscles. *Nature*, 2019, 575: 324–329
- 15 Chukewad Y M, James J, Singh A, et al. Robofly: An insect-sized robot with simplified fabrication that is capable of flight, ground, and water surface locomotion. *IEEE Trans Robot*, 2021, 37: 2025–2040
- 16 James J, Iyer V, Chukewad Y, et al. Liftoff of a 190 mg laser-powered aerial vehicle: The lightest wireless robot to fly. In: Proceedings of the 2018 IEEE International Conference on Robotics and Automation (ICRA). Brisbane, QLD: IEEE, 2018. 3587–3594
- 17 Chukewad Y M, Singh A T, James J M, et al. A new robot fly design that is easier to fabricate and capable of flight and ground locomotion. In: Proceedings of the 2018 IEEE/RSJ International Conference on Intelligent Robots and Systems (IROS). Madrid: IEEE, 2018. 4875–4882
- 18 Fuller S B. Four wings: An insect-sized aerial robot with steering ability and payload capacity for autonomy. *IEEE Robot Autom Lett*, 2019, 4: 570–577
- 19 Hoff J, Syed U, Ramezani A, et al. Trajectory planning for a bat-like flapping wing robot. In: Proceedings of the 2019 IEEE/RSJ International Conference on Intelligent Robots and Systems (IROS). Macau: IEEE, 2019. 6800–6805
- 20 de Croon G C H E, de Clercq K M E, Ruijsink R, et al. Design, aerodynamics, and vision-based control of the delfly. *Int J Micro Air Vehicles*, 2009, 1: 71–97
- 21 de Croon G C H E, Perçin M, Remes B D W, et al. The DelFly. Dordrecht: Springer Netherlands, 2016
- 22 Karásek M, Muijres F T, De Wagter C, et al. A tailless aerial robotic flapper reveals that flies use torque coupling in rapid banked turns. *Science*, 2018, 361: 1089–1094
- 23 Fei F, Tu Z, Yang Y, et al. Flappy hummingbird: An open source dynamic simulation of flapping wing robots and animals. In: Proceedings of the 2019 International Conference on Robotics and Automation (ICRA), 2019. 9223–9229
- 24 Phan H V, Kang T, Park H C. Design and stable flight of a 21 g insect-like tailless flapping wing micro air vehicle with angular rates feedback control. *Bioinspir Biomim*, 2017, 12: 036006
- 25 Chin Y W, Kok J M, Zhu Y Q, et al. Efficient flapping wing drone arrests high-speed flight using post-stall soaring. *Sci Robot*, 2020, 5: eaab2386
- 26 Rosen M H, le Pivain G, Sahai R, et al. Development of a 3.2 g untethered flapping-wing platform for flight energetics and control experiments. In: Proceedings of the 2016 IEEE International Conference on Robotics and Automation (ICRA). Stockholm: IEEE, 2016. 3227–3233
- 27 Phan H V, Park H C. Mechanisms of collision recovery in flying beetles and flapping-wing robots. *Science*, 2020, 370: 1214–1219
- 28 Hines L, Campolo D, Sitti M. Liftoff of a motor-driven, flapping-wing microaerial vehicle capable of resonance. *IEEE Trans Robot*, 2014, 30: 220–232
- 29 Zou Y, Zhang W, Zhang Z. Liftoff of an electromagnetically driven insect-inspired flapping-wing robot. *IEEE Trans Robot*, 2016, 32: 1285–1289
- 30 Wang C, Zhang W, Zou Y, et al. A sub-100 mg electromagnetically driven insect-inspired flapping-wing micro robot capable of liftoff and control torques modulation. *J Bionic Eng*, 2020, 17: 1085–1095
- 31 Wang C, Zhang W, Hu J, et al. A modified quasisteady aerodynamic model for a sub-100 mg insect-inspired flapping-wing robot. *Appl Blon Biomech*, 2020, 2020: 1–12
- 32 Wood R J. The First takeoff of a biologically inspired at-scale robotic insect. *IEEE Trans Robot*, 2008, 24: 341–347
- 33 Wood R J, Avadhanula S, Sahai R, et al. Microrobot design using fiber reinforced composites. *J Mech Des*, 2008, 130: 052304
- 34 Sane S P. The aerodynamics of insect flight. *J Exp Biol*, 2003, 206: 4191–4208
- 35 Wang Z J. Dissecting insect flight. *Annu Rev Fluid Mech*, 2005, 37: 183–210
- 36 Dickinson M H, Lehmann F O, Sane S P. Wing rotation and the aerodynamic basis of insect flight. *Science*, 1999, 284: 1954–1960
- 37 Srygley R B, Thomas A L R. Unconventional lift-generating mechanisms in free-flying butterflies. *Nature*, 2002, 420: 660–664
- 38 Wood R J, Avadhanula S, Menon M, et al. Microrobotics using

- composite materials: The micromechanical flying insect thorax. In: Proceedings of the 2003 IEEE International Conference on Robotics and Automation (Cat. No.03CH37422). Taipei: IEEE, 2003. 1842–1849
- 39 Steltz E, Avadhanula S, Fearing R S. High lift force with 275 Hz wing beat in MFI. In: Proceedings of the 2007 IEEE/RSJ International Conference on Intelligent Robots and Systems. San Diego: IEEE, 2007. 3987–3992
- 40 Finio B M, Whitney J P, Wood R J. Stroke plane deviation for a microrobotic fly. In: Proceedings of the 2010 IEEE/RSJ International Conference on Intelligent Robots and Systems. Taipei: IEEE, 2010. 3378–3385
- 41 Finio B M, Wood R J. Distributed power and control actuation in the thoracic mechanics of a robotic insect. *Bioinspir Biomim*, 2010, 5: 045006
- 42 Truong N T, Phan H V, Park H C. Design and demonstration of a bio-inspired flapping-wing-assisted jumping robot. *Bioinspir Biomim*, 2019, 14: 036010
- 43 Wood R J, Steltz E, Fearing R S. Optimal energy density piezoelectric bending actuators. *Sens Actuat A-Phys*, 2005, 119: 476–488
- 44 Mukundarajan H, Bardon T C, Kim D H, et al. Surface tension dominates insect flight on fluid interfaces. *J Exp Biol*, 2016, 219: 752–766
- 45 Zhou S, Zhang W, Zou Y, et al. Piezoelectric driven insect-inspired robot with flapping wings capable of skating on the water. *Electron Lett*, 2017, 53: 579–580
- 46 Dadfarnia M, Jalili N, Xian B, et al. Lyapunov-based vibration control of translational Euler-Bernoulli beams using the stabilizing effect of beam damping mechanisms. *J Vib Control*, 2004, 10: 933–961
- 47 Dadfarnia M, Jalili N, Xian B, et al. A Lyapunov-based piezoelectric controller for flexible Cartesian robot manipulators. *J Dynamic Syst Measurement Control*, 2004, 126: 347–358
- 48 Chen Y, Ma K, Wood R J. Influence of wing morphological and inertial parameters on flapping flight performance. In: Proceedings of the 2016 IEEE/RSJ International Conference on Intelligent Robots and Systems (IROS), 2016. 2329–2336
- 49 St. Pierre R, Bergbreiter S. Toward autonomy in sub-gram terrestrial robots. *Annu Rev Control Robot Auton Syst*, 2019, 2: 231–252